Journal of Applied Physics

RESEARCH ARTICLE | FEBRUARY 20 2026

Modulating charge transport via 2 MeV He^+ irradiation in VO_2

Rebeca M. Gurrola ; Adelaide Bradicich ; Fatme Jardali ; John M. Cain ; Timothy D. Brown ; Jenny L. Chong; John Ponis ; Sangheon Oh ; Ryan M. Schoell ; Digvijay R. Yadav; Jiaqi Dong; Christopher M. Smyth ; Matt Pharr ; Suhas Kumar ; Kelvin Xie ; Sarbajit Banerjee ; Khalid Hattar ; A. Alec Talin ; Tzu-Ming Lu ; Patrick J. Shamberger

J. Appl. Phys. 139, 075107 (2026)
https://doi.org/10.1063/5.0312581

Journal of Applied Physics ARTICLE pubs.aip.org/aip/jap

Modulating charge transport via 2 MeV He^+ irradiation in VO_2

Cite as: J. Appl. Phys. **139**, 075107 (2026); doi: 10.1063/5.0312581
Submitted: 17 November 2025 · Accepted: 30 January 2026 ·
Published Online: 20 February 2026

Rebeca M. Gurrola,[1] Adelaide Bradicich,[2] Fatme Jardali,[1] John M. Cain,[3] Timothy D. Brown,[4] Jenny L. Chong,[1] John Ponis,[5] Sangheon Oh,[4] Ryan M. Schoell,[2] Digvijay R. Yadav,[1] Jiaqi Dong,[1] Christopher M. Smyth,[3] Matt Pharr,[6] Suhas Kumar,[4] Kelvin Xie,[1] Sarbajit Banerjee,[5] Khalid Hattar,[2,7] A. Alec Talin,[4] Tzu-Ming Lu,[2] and Patrick J. Shamberger[1,a)]

AFFILIATIONS

[1]Department of Materials Science and Engineering, Texas A&M University, College Station, Texas 77843, USA
[2]Center for Integrated Nanotechnologies, Sandia National Laboratories, Albuquerque, New Mexico 87123, USA
[3]Sandia National Laboratories, Albuquerque, New Mexico 87185, USA
[4]Sandia National Laboratories, Livermore, California 94550, USA
[5]Department of Chemistry, Texas A&M University, College Station, Texas 77843, USA
[6]Department of Mechanical Engineering, Texas A&M University, College Station, Texas 77843, USA
[7]Department of Nuclear Engineering, University of Tennessee, Knoxville, Tennessee 37996, USA

[a)]**Author to whom correspondence should be addressed:** patrick.shamberger@tamu.edu

ABSTRACT

Vanadium dioxide (VO_2) is of interest for adaptive electronic applications such as neuromorphic neuristor devices and variable emissivity or tunable thermal control materials, thanks to its key property—a metal–insulator transition (MIT) at 68 °C that is accompanied by a dramatic change in electrical and optical properties. To improve performance in these roles, it is critical to develop approaches to engineer transport properties and the MIT behavior. While many documented techniques exist to modulate the MIT and film resistivities via lattice strain and chemical doping, less is known about the effects of ion irradiation on the intrinsic properties of VO_2, despite the ability to control the spatial distribution of irradiation beams and the prevalence of high energy ion implantation in the semiconductor industry. The impact of irradiation of different acceleration energies on the responses of VO_2 is of specific interest, as charged particle energy generally impacts both the resulting defect profile and corresponding transport behavior. Here, we demonstrate that 2 MeV He ions at equivalent calculated displacements per atom, in two different types of films, can create remarkable changes to the nature of charge transport in VO_2, especially in the low-temperature insulating phase. Simulation of resulting changes in electrical conductivity reveals that He ion irradiation offers a strategy to increase both oscillation frequency and the signal transmission. These results provide insights into the intentional design of defect populations to modulate transport for neuromorphic VO_2 devices.

I. INTRODUCTION

Vanadium dioxide (VO_2) is a candidate material for neuronal emulation in neuromorphic devices due to its dynamical nonlinear resistance switching behavior resulting from its metal–insulator transition (MIT).[1] This nonlinear switching allows such devices to amplify small fluctuations when electrically biased, resulting in electrical (and thermal) self-oscillations.[2] Realization of VO_2 as a neuronal element requires control over the ratio of the electrical conductivities in the on and off device states (on/off ratio), hysteresis, and the absolute conductivities of the insulating and metallic phases, as these intrinsic properties dictate the negative differential resistance (NDR) observed in the device's electrical response.

While many studies have investigated the use of lattice strain and chemical doping to alter the MIT and the transport properties of VO_2,[3–5] few studies have investigated the effect of ion irradiation to induce a desired change in the electronic properties of these

adaptive electronic films. Specifically, the impacts of irradiation fluence and ion energy on temperature-dependent charge transport in VO_2 as a function of irradiation energy remain unclear, despite the common use of implantation to modify transport properties of semiconductors like Si.[6] Modifying the on/off ratio and the temperature/voltage hysteresis is essential for implementing VO_2 in neuronal devices. For instance, the large on/off ratio of VO_2 leads to a small temperature range where oscillations are possible (roughly 60.85–62.85 °C) compared to NbO_2 (roughly 44.85–806.85 °C).[2,7] This effect is due to the large change in conductance over a small temperature range (i.e., electrical and thermal non-linearities are highly coupled), which also leads to higher probabilities of damaging the device by overheating. Given the small temperature range over which VO_2 can oscillate, the modulation of its temperature-dependent electrical and thermal transport as well as MIT properties can broaden this regime of utility.

One route to broaden the operating temperature range for VO_2 devices is to alter its MIT characteristics. The MIT of VO_2 is strongly influenced by stoichiometry, as oxygen deficiency causes the low-temperature insulating phase of VO_2 to become less resistive due to the addition of carriers from oxygen vacancies.[4] Additionally, the transition temperature, T_{MIT}, decreases with oxygen deficiency although the amount of oxygen that causes this effect is hard to pinpoint.[8–10] Similar effects are obtained with the introduction of defects, i.e., the resistivity of the insulating phase decreases due to the addition of carriers and the resistivity of the metallic phase increases due to the reduction in carrier mobility via defect creation.[11] This effect can vary when defects are introduced by irradiation, as defect densities can change depending on parameters including irradiation dose, energy, ion choice, and sample thickness.

Point defects, specifically oxygen vacancies, are commonly introduced by irradiation, but few studies document the interplay between irradiation defects and the use of irradiation to introduce charge carriers in VO_2.[12] Oxygen ion (O^+) irradiation (70–250 keV) of VO_2 on (0001) Al_2O_3 has been shown to result in a 12 °C reduction in the MIT temperature and a half order-of-magnitude reduction in the resistivity of the insulating phase ($\rho_{insulating}$).[13] In a separate study, the transformation was significantly modified by creating gradients of ion concentrations in the VO_2 films from a double implantation of Ne^+ at 100 and 50 keV at fluences of 2×10^{14}–3×10^{14} ions/cm^2.[14] Interestingly, the films transformed completely in three separate steps with the first starting at the same temperature as the control sample. This effect was attributed to the Gaussian like distribution of Ne^+ in VO_2 resulting in lattice strain as confirmed by x-ray diffraction (XRD). Further area-selective ion implantation achieved a patterned insulating and metallic film at room temperature.

To this end, we prepared polycrystalline and quasi-epitaxial VO_2 films on SiO_2/Si and on c-plane Al_2O_3 (0001) substrates, respectively, and systematically investigated the effects of 2 MeV He irradiation on the electrical transport properties and on the MIT characteristics. To provide insights into the changes that these effects would ultimately produce in the electrical response of a device, simulations using a compact model of a relaxation oscillator were performed to investigate changes to VO_2 oscillation behaviors to gain insights into their ultimate application in producing artificial spiking neural functions. Comparing the effects of low-energy irradiation (previous work)[12] and high energy irradiation (present work) reveals that low-energy He ion irradiation is most effective in changing the properties of the textured film, resulting in the greatest net changes to the frequencies and $\Delta V/\Delta T$ performance metrics of the oscillations.

II. METHODS

A. Thin film deposition, device fabrication, and irradiation

We deposited 100 nm VO_2 thin films using reactive DC magnetron sputtering. For this study, we studied two thin films deposited on c-plane Al_2O_3 (0001) (to obtain quasi-epitaxial VO_2) and two thin films deposited on 100 nm SiO_2 on Si (001) (to obtain polycrystalline VO_2). We then characterized the crystal structures and morphologies of the thin films using x-ray diffraction (XRD), scanning electron microscopy (SEM) (Fig. S1 in the supplementary material), atomic force microscopy (AFM) (Fig. S2 in the supplementary material), Raman spectroscopy (Fig. S3 in the supplementary material), transmission electron microscopy (TEM) (Fig. S4 in the supplementary material), and x-ray absorption near-edge structure (XANES) spectroscopy (Fig. S5 in the supplementary material). Characterization details are provided in the supplementary material. Quasi-epitaxial is used to describe the texture of the VO_2 on Al_2O_3 substrate, which is highly textured but not perfectly a single crystal as described previously.[12] We next fabricated planar four-terminal devices using a multi-step lithography process described previously.[12] An initial round of transport studies was conducted on these samples to provide reference or "control sample" metrics.

After fabrication, the VO_2 devices were subjected to 2 MeV He^+ ion irradiation using the 3 MV Tandem Pelletron accelerator at the Ion Beam Laboratory housed at Sandia National Laboratories. We chose the 2 MeV acceleration energy of the He^+ ions based on simulations of depth profiles using the Stopping and Range of Ions in Matter (SRIM) software.[15] SRIM simulations predict that 2 MeV He ions pass fully through the VO_2 thin films (Figs. S6 and S7 in the supplementary material), resulting in no doping and predominately create Frenkel defects (single vacancy and self-interstitial pairs). Displacements per atom (dpa) was calculated for each fluence step (Fig. S6 in the supplementary material) and is listed in Table I. Samples were subjected to increasing cumulative irradiation fluences (Table I), and between each exposure, specific devices were reanalyzed to avoid device-to-device variability.

B. Structural characterization

We performed x-ray absorption near-edge structure (XANES) measurements of V L- and O K-edge XANES measurements at beamline 7-ID−1 of the National Synchrotron Light Source II at Brookhaven National Laboratory, operated by the National Institute of Standards and Technology. A grid bias of −500 V was used to reject low-energy electrons and reduce noise. A charge compensation gun was used to avert sample charging. The data were collected with a resolution of 0.2 eV (Fig. S5 in the supplementary material). The partial electron yield (PEY) signals were normalized to the incident beam intensity measured from a

TABLE I. Irradiation conditions utilized in this study, including cumulative fluence after each step. In bold is the ID to reference the data.

		Step 1		Step 2		Step 3	
Substrate	Energy (MeV)	Fluence (ions cm^{-2})	dpa[a]	Fluence (ions cm^{-2})	dpa[a]	Fluence (ions cm^{-2})	dpa[a]
SiO_2/Si	2	3×10^{15} **P-3S-F1**	1.88×10^{-3}	3×10^{16} **P-3S-F2**	2.07×10^{-2}	5×10^{16} **P-3S-F3**	5.21×10^{-2}
SiO_2/Si	2	1×10^{16} **P-2S-F1**	6.28×10^{-3}	5×10^{16} **P-2S-F2**	3.77×10^{-2}	0	n/a
Al_2O_3 (0001)	2	3×10^{15} **E-3S-F1**	1.88×10^{-3}	3×10^{16} **E-3S-F2**	2.07×10^{-2}	5×10^{16} **E-3S-F3**	5.21×10^{-2}
Al_2O_3 (0001)	2	1×10^{16} **E-2S-F1**	6.28×10^{-3}	5×10^{16} **E-2S-F2**	3.77×10^{-2}	0	n/a

[a]Cumulative dpa (calculated by SRIM) after each fluence step.

freshly evaporated gold mesh. The spectra were pre-to-post-edge normalized using the ATHENA software package[16] and energy-calibrated to the $V3d_{xy}$ feature in the V L_3-edge spectrum of a fresh V_2O_5 standard (Aldrich ≥99.6%).

C. Electrical characterization

Transport, Seebeck, and noise measurements (Fig. S8 in the supplementary material) were performed on planar four-terminal devices as described previously.[12] Hall measurements were performed on patterned Hall bars wire bonded to a dual-inline-package header and measured in a sample-in-vapor variable temperature system, in which the sample temperature was varied from 49.85 to 84.85 °C, covering the metal–insulator transition of VO_2. Low-frequency (3–13 Hz) lock-in techniques are used to measure the longitudinal and transverse magnetoresistances as a function of magnetic field. The magnetic field is swept between ±1 T. The Hall density and Hall mobility are calculated from magnetoresistances. While we tried to perform Hall measurements on polycrystalline films, we found the resistance of these films was too high for our measurement setup. Thus, Hall measurement data are only presented for the quasi-epitaxial films.

D. Compact model

To investigate the impact of irradiation-altered device properties on the behaviors of materials in one application, artificial neurons, we used a physics-based compact model[17] to simulate electro-thermal oscillator dynamics. These simulations link the temperature-dependent electrical and thermal properties of the films to nonlinear oscillations via local activity theory.

The temperature-dependent electrical conductivities were obtained from the scaled electrical resistance data [Figs. 6(a) and 6(b)], while values for thermal conductivity[18] and specific heat capacity[19] were obtained from the literature. Thermal conductivity values were obtained from undoped VO_2 pellets since no thermal transport measurements exist for irradiated thin film VO_2 devices. Therefore, we used bulk, undoped values as a conservative baseline intended to capture the intrinsic lattice-dominated thermal transport of VO_2. These datasets were fit to a sigmoidal function, a power series with a first-order phase transition (FOPT), and the Debye function with a FOPT. The compact model employs a coupled system of two first-order differential equations: (1) Kirchoff's voltage law for electrical oscillations and (2) Joule heating and Newton's law of cooling for thermal oscillations, solving these equations with a Runge–Kutta numerical integrator. Capacitance-dependent oscillation frequency and the amplitudes of electrical and thermal oscillations were simulated at an ambient temperature of 26.85 °C for lateral device dimensions of L = 40 μm, W = 15 μm, H = 0.1 μm, on the scale of the experimental devices. These metrics were extrapolated to larger capacitances and projected onto a circuit capacitance constraint of 100 pF.

In the present compact model, acoustic coupling to the substrate is not included. The active layer is treated as a lumped thermal system that exchanges heat directly with an ambient thermal reservoir, without explicitly accounting for the substrate, interfacial thermal resistances, or phonon transmission effects. Consequently, the spiking frequencies predicted by our model are likely overestimates, while the ratio of voltage amplitude to temperature amplitude ($\Delta V/\Delta T$) is underestimates. Additionally, the compact model does not account for microstructural changes but does capture (1) the dependence of electrical and thermal transport properties of the device active material and (2) external design constraints. Since the electrical transport characteristics of the irradiated devices are taken directly from our measurements, and because, overall, the relative changes of electrical transport with temperature are orders of magnitude larger than those of thermal transport, we expect variations in the temperature dependence of the electrical conductance to play a dominant role in determining differences in neuronal performance among different irradiated VO_2 devices.

III. RESULTS

A. Electrical transport in 2 MeV He irradiated films

1. Temperature-dependent electrical resistivity

To determine the effects of high energy irradiation on the transport properties of VO_2, we first measured the electrical resistivities as a function of temperature, ρ(T), of four VO_2 thin films—two polycrystalline and two quasi-epitaxial films, with each film

containing a total of three and four devices, respectively. We next irradiated the four thin films in a series of steps, thermally cycling the films 15 times after each step to eliminate virgin cycling effects before measuring ρ(T) for each device. Of the two thin films of each type, one was irradiated in three fluence steps and one was irradiated in two fluence steps, with the last step for all films being the same fluence (5×10^{16}) (Fig. 1, Table I). To reference different samples, irradiation steps, or both, samples will be referred to in

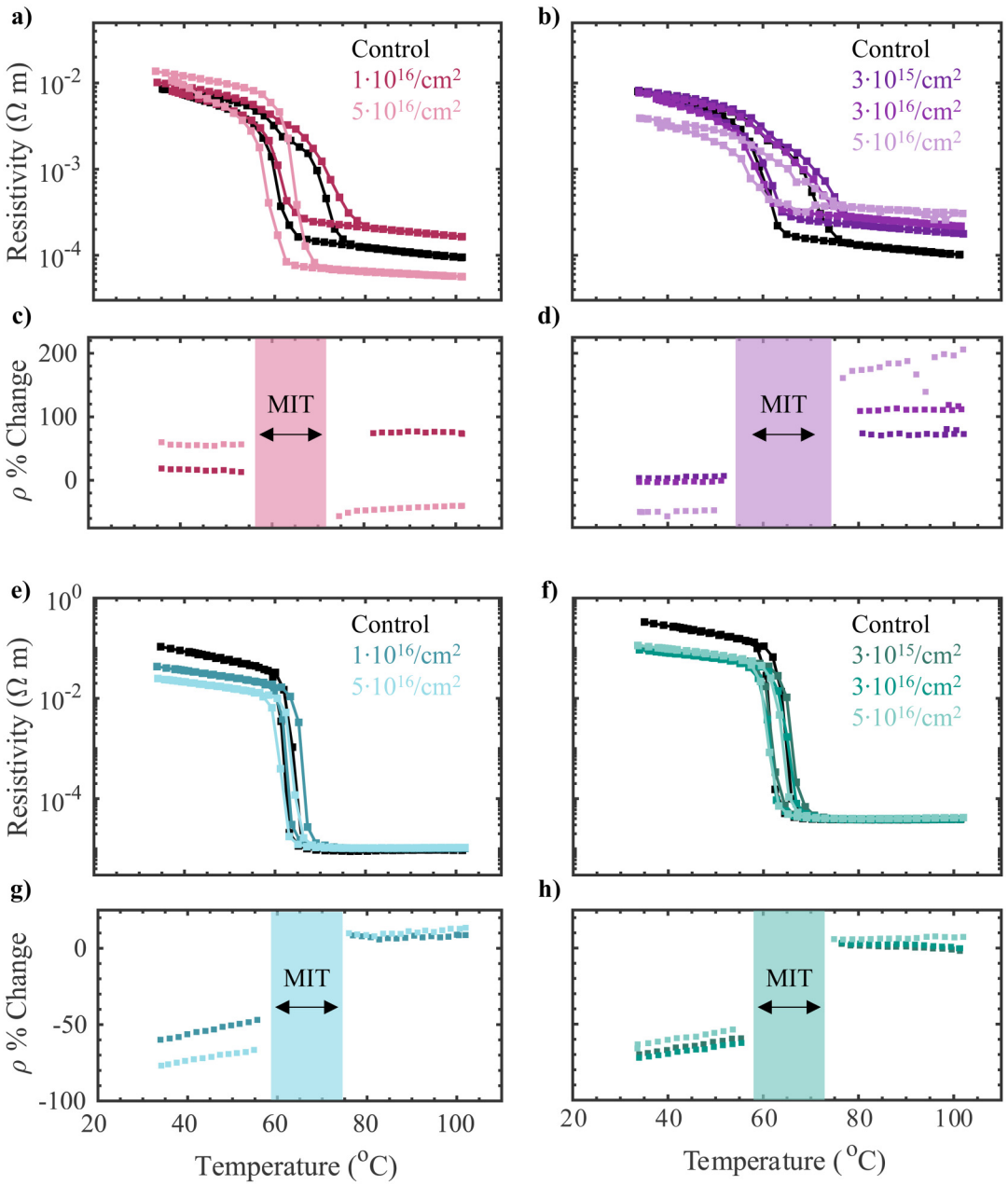

FIG. 1. Four-point transport measurements of irradiated VO_2 on (a)–(d) SiO_2/Si (polycrystalline) and VO_2 on (e)–(h) Al_2O_3 (quasi-epitaxial) films. Hysteresis loop of resistivity vs temperature before and after 2 MeV irradiation for samples deposited on (a) and (b) SiO_2/Si and (e) and (f) Al_2O_3 for different fluences. Measurements for the as-deposited (control) film is plotted in black. Change in the resistivity of the films upon irradiation for VO_2 on (c) and (d) SiO_2/Si and (g) and (h) Al_2O_3 substrate. For all measurements, the same device was irradiated and then measured to eliminate device-to-device variability.

the following format: type of film (P for poly or E for quasi-epitaxial)-number of irradiation steps (3S for three steps or 2S for two steps)-fluence step (first fluence F1 or second fluence F2 or third fluence F3). For instance, the polycrystalline film measured after the third irradiation out of three steps would be referred to as P-3S-F3.

Displacements per atom (dpa) was adopted as a standard measure of irradiation damage in materials to account for total accumulated damage after each fluence step. Measurements were obtained within a day of irradiation to prevent aging effects and were cycled up to fifteen times after each irradiation exposure to eliminate virgin cycling effects prior to the collection of data presented and used for analysis throughout this study. Qualitatively, both quasi-epitaxial films are similarly impacted by irradiation in the low-temperature insulating phase with overall $\rho_{insulating}$ decreasing by similar amounts and $\rho_{metallic}$ showing no change. However, the polycrystalline films exhibit opposing trends for $\rho_{insulating}$ and $\rho_{metallic}$ when comparing two-step and three-step irradiation.

The average change in resistivity, relative to pre-irradiation resistivity, was calculated as a function of dpa after each irradiation step (Table I, Fig. 2). We calculated the changes in resistivities with respect to the control (unirradiated) measurements from the temperature-dependent resistivity measurements. To eliminate variability from the temperature dependence of resistivities, we used the resistivities selected from only one temperature for the insulating (35 °C) and metallic phases (100 °C) for each device. Then, the averaged percent changes in resistivities were calculated at each fluence step, averaged for three (polycrystalline) or four (quasi-epitaxial) devices, and their standard deviations (Fig. 2).

The polycrystalline and quasi-epitaxial films have opposing trends with respect to resistivity changes after irradiation. For the polycrystalline film in its insulating phase, subsequent irradiation

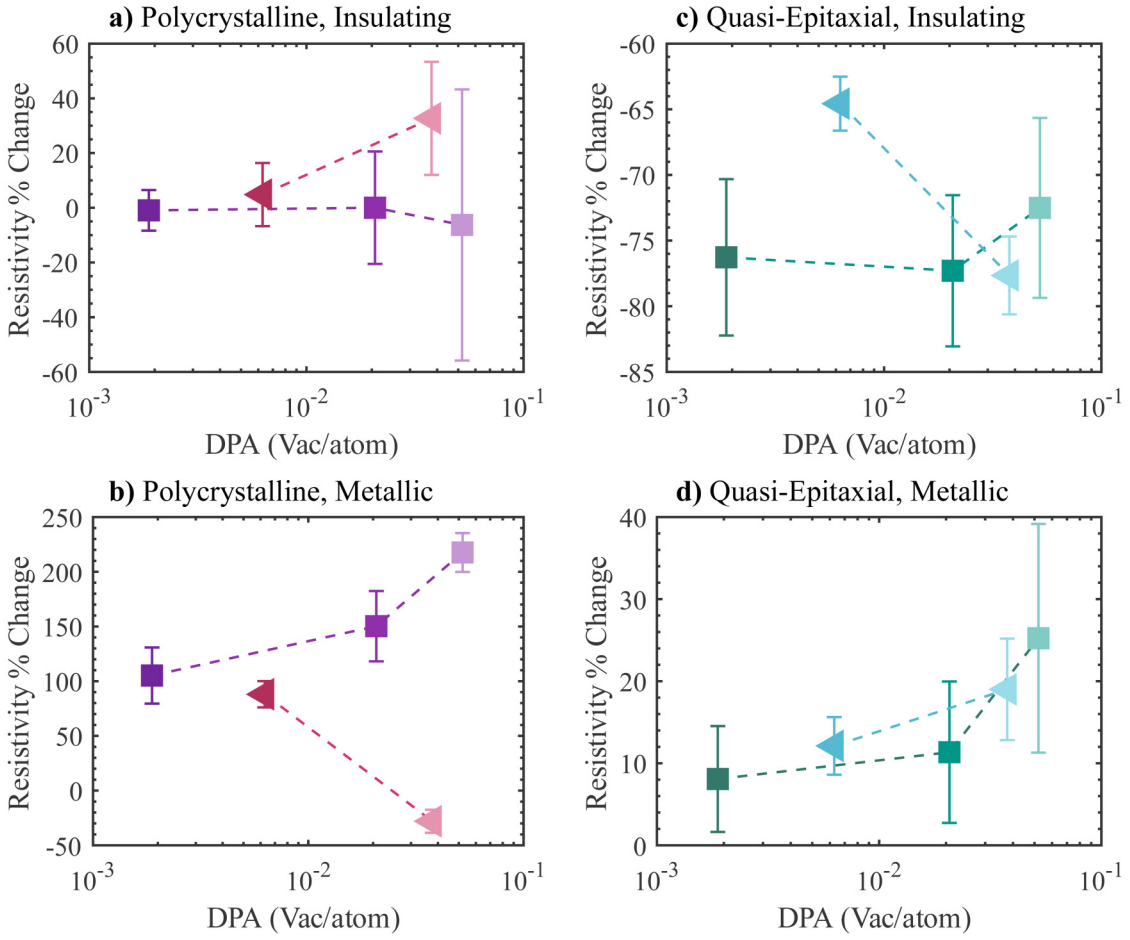

FIG. 2. Change in resistivity of films upon irradiation for (a) and (b) SiO_2/Si substrate (polycrystalline film) and (c) and (d) Al_2O_3 substrate (quasi-epitaxial film). Trends in resistivity with increasing fluence for high (HE) He irradiation energy plotted against dpa are compared for (a) and (c) insulating M_1 phase and (b) and (d) metallic R phase. Each data point represents the average resistivity change (%) of four devices taken on the same film. Colors are included to group data points. Square markers are used to indicate films irradiated in three steps, while triangle markers are used to indicate films irradiated in two steps.

steps result in minor changes, with resistivity increasing up to 32% in two steps (P-2S-F2) [Fig. 2(a)]. However, in its metallic phase [Fig. 2(b)], regardless of the number of irradiations, the first step results in an increase in resistivity up to 100%. For irradiation in two steps, at the second fluence step (P-2S-F2), all devices showed a decreased ΔT_{MIT} and an on/off ratio like the control measurement. Films irradiated in three steps did not show this trend despite being irradiated at the same fluence for the last step (5×10^{16}) and resulted in a 217% change relative to the control measurements (P-3S-F3).

The resistivity of the insulating phase of the quasi-epitaxial film decreased substantially with the first step (−64% and −76%) but changed little with additional irradiation (E-2S-F1 and E-3S-F1). Interestingly, although dpa continues to increase, the resistivity % change in the quasi-epitaxial film exhibits saturation, indicating a threshold-type response to damage accumulation [Fig. 2(c)]. The resistivity ($\rho_{metallic}$) of the metallic phase increased monotonically with dpa from 8% (E-3S-F1) change to 25% (E-3S-F3) and 12% (E-2S-F1) change to 19% (E-2S-F2) in Fig. 2(d); however, this effect is more dramatic in polycrystalline films with resistivity percent change increasing from 100% to 200% for irradiation in three steps (P-3S-F3).

From these electrical resistivity trends, three important observations are evident: (1) The differences in irradiation procedure are important, as seen in the differences in behaviors for these processes in which irradiation is performed in two steps vs three steps, (2) a substrate effect (polycrystalline vs quasi-epitaxial) is pronounced, and (3) we find that changes to the resistivity of the insulating phase do not scale with damage (dpa).

To quantify the changes to the characteristics of the metal–insulator transition upon irradiation, we inverted the measured electrical resistivities to study electrical conductivity and subsequently fit that data [Figs. 3(a)–3(d)] to a sigmoidal function to determine the change in the critical temperature upon heating (ΔT_H), the change in the critical temperature upon cooling (ΔT_C), the width of transition upon heating (ΔW_H), and the width of transition upon cooling (ΔW_C). Details of the fitting procedure are described in the supplementary material.

We found that ΔT_H and ΔT_C are asymmetrically affected by irradiation in polycrystalline films with ΔT_H changing by 5 °C compared to 2 °C of ΔT_C. However, irradiation from step 1 to the final second step results in the largest difference [Fig. 3(e)] 1.5 to −5.9 °C for ΔT_H compared to irradiation in three steps, which plateaus from 3.8 to 1 °C. ΔT_C in two steps changes from 0.1 to −1.3 °C, similar to the change in three steps from 0.3 to −1.7 °C in Fig. 3(g). Irradiation in three steps results in an increasing trend for both ΔW_H, ΔW_C and a decreasing trend for two steps in Figs. 3(i) and 3(k).

Upon inspection, we found that the change in ΔT_H and ΔT_C follows the same decreasing trend for quasi-epitaxial films as with the polycrystalline films. Additionally, irradiation in two steps resulted in the greatest difference in ΔT_H and ΔT_C from the first to second steps, unsurprising given the larger fluence and dpa of this step. The width of transformation similarly decreases overall for ΔW_H and ΔW_C with very little change occurring.

Through quantifying the changes to the transformation, three key observations emerge: (1) In all cases, by the third irradiation step, ΔT_H and ΔT_C are independent of dpa; (2) for quasi-epitaxial films, two steps results in greater ΔT_H and ΔT_C changes; and (3) for polycrystalline films, the heating transformation from monoclinic to rutile (M1 to R phase) is affected to a greater degree than the cooling transformation.

2. Seebeck measurements

In order to obtain deeper insights into the interactions between irradiation-induced defects and charge transport, we performed Seebeck measurements of the low-temperature insulating VO_2 phase in the polycrystalline and quasi-epitaxial thin films (Fig. 4). To ensure the reproducibility of the measurements, three devices were measured on each thin film. Seebeck measurements are performed by measuring the change in voltage (ΔV) as a function of change in temperature (ΔT). The Seebeck coefficient is obtained from applying a linear fit to the data (Table II).

The Seebeck coefficient of VO_2 has been well documented for both of its phases, with electrons as the majority carriers and the coefficient varying from −17 to −400 μV/K.[20,21] We found that the control measurements of the polycrystalline films exhibit an average negative Seebeck coefficient of $-236 \pm 22\,\mu$V/K [Fig. 4(a)]. For the quasi-epitaxial films, the films also consistently display an average negative Seebeck coefficient of $-9.9 \pm 0.2\,\mu$V/K. From the Seebeck data presented above, we can infer that the irradiation similarly effects the polycrystalline and quasi-epitaxial films with both values remaining negative.

3. Hall measurements

To quantify changes to the carrier density and mobility of the films pre- and postirradiation, Hall measurements were performed on the quasi-epitaxial films. Due to high electrical resistances, we were only able to perform these measurements on the unirradiated quasi-epitaxial films and after the second irradiation step at 3×10^{16} (E-3S-F2). Measurements were obtained at 49.85 °C for its insulating phase and at 84.85 °C for its metallic phase. Carriers are confirmed to be electrons due to the negative slope of R_{xy} under a negative magnetic field. Hall carrier density and mobilities obtained are consistent with literature values.[20,22,23] After irradiation, the mobility of the charge carriers increases by 93% in the insulating phase but decreases by 25% in the metallic phase. Similarly, the carrier density increases by 36% in the insulating phase but decreases by 15% in the metallic phase. From these observations, we infer that, for quasi-epitaxial films, (1) irradiation has a greater impact on the charge carrier density and mobility in the insulating phase than the metallic phase; and (2) irradiation-induced defects alter the mobility to a greater degree than the carrier density.

The significant (93%) increase in charge mobility with irradiation is somewhat counterintuitive, since the creation of defects generally leads to increased scattering. One potential explanation for this observation relates to the impact of lattice strain on charge carrier mobility. From previous reports, He^+ irradiation has been observed to expand the out-of-plane lattice constant in $SrVO_3$, SnO_2, and $La_{0.7}Sr_{0.3}MnO_3$ epitaxial thin films.[24–27] This lattice strain effect was also observed previously with Ne^+ irradiation of epitaxial VO_2 on (0001) Al_2O_3.[14] From first principles density of states (DOS) calculations, the resulting bandgap diagram showed

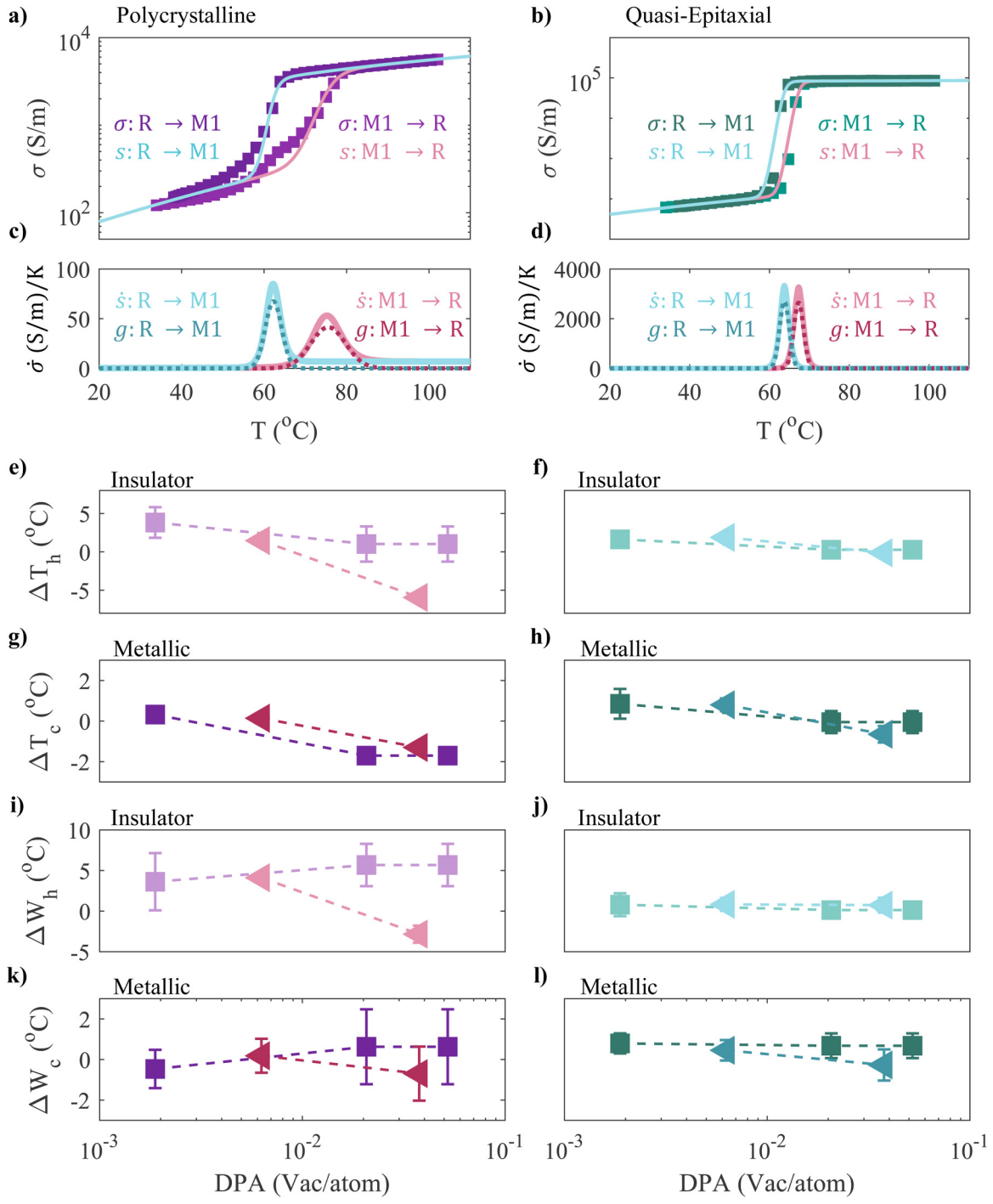

FIG. 3. Conductivity σ(T) fitted to a sigmoid function (***s***) for the heating insulating and cooling metallic phases of VO_2 for (a) polycrystalline and (b) quasi-epitaxial films. Derivative of conductivity (***ṡ***) fitted to a Gaussian (***g***) for both heating and cooling runs for (c) polycrystalline and (d) quasi-epitaxial films. Average change in critical temperatures (ΔT_H, ΔT_C) reflecting the 50% transition of the Gaussian function for (e) and (f) heating and (g) and (h) cooling of the polycrystalline and quasi-epitaxial films relative to their respective control films. Average change in the transition widths (ΔW_H, ΔW_C) was obtained using the FWHM of the Gaussian fit to the sigmoid function for both (i) and (j) heating and (k) and (l) cooling transitions relative to the control films.

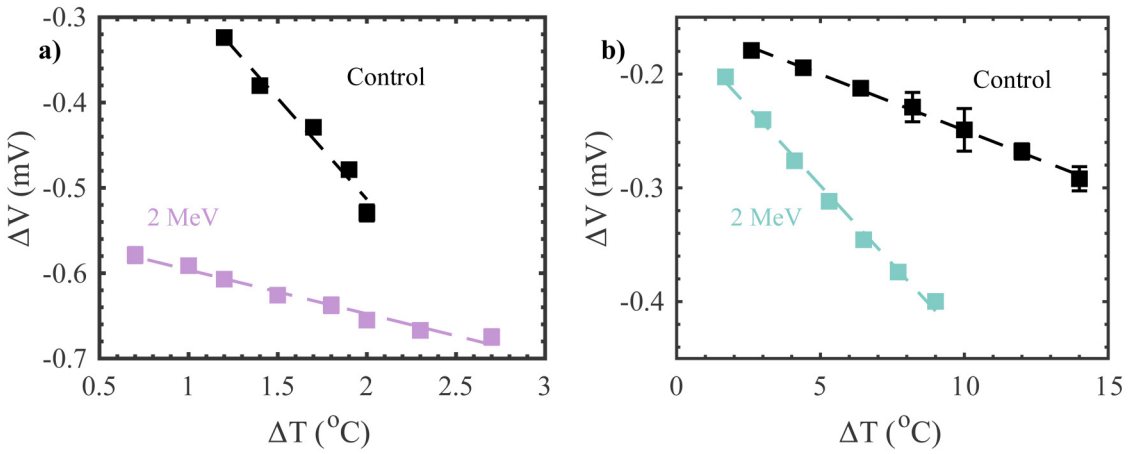

FIG. 4. Seebeck measurements of the irradiated insulating M1 VO_2 phase on (a) the SiO_2/Si substrate (polycrystalline film) and (b) Al_2O_3 substrate (quasi-epitaxial film). Values for the unirradiated control are plotted in black. Seebeck measurements for films He irradiated in three steps at 2 MeV at fluences (a) 5×10^{16} ions/cm^2 and (b) 5×10^{16} ions/cm^2 are indicated by dashed lines and square markers with dashed lines, respectively.

an upward shift of the $d_{//}$* orbital and downward shifts of the $d_{//}$ and π* bands.[14] Similarly, the use of lattice strain to compress or stretch the c-axis of rutile VO_2 resulted in bandgap modifications.[28–30] Thus, one explanation to the observed change in mobility is that the lattice strain resulting from irradiation modified the band structure of VO_2 and consequently the carrier mobility.

B. Effects of 2 MeV He irradiation on local structure

The electronic structure of the control and irradiated polycrystalline films was investigated using X-ray Absorption Near-edge Structure (XANES) spectroscopy. XANES spectroscopy provides element-specific insight into the local electronic structure of unoccupied and partially occupied (conduction band) states. Data were collected only on the polycrystalline films, both before and after the high energy irradiation at two fluence steps (1×10^{16}, 5×10^{16} ions cm^{-2}). Figure 5 presents the oxygen K-edge XANES data, displaying both the partial electron yield (PEY) and total fluorescence yield (TFY), with TFY providing a more accurate representation of the bulk sample due to the longer mean free path of fluorescence photons compared to photoelectrons. The vanadium L-edge spectra correspond to dipole-allowed transitions from V 2p core levels to hybrid V—O 3d states and are dominated by multiplet effects. These spectra show negligible differences between the control and the irradiated film, suggesting very little change in the vanadium crystal field splitting or oxidation state [Fig. S5(a) in the supplementary material].[31,32] The oxygen K-edge spectra correspond to transitions from O 1*s* core levels to O 2*p* states hybridized with V 3*d* and 4*sp* states and show two manifolds consistent with crystal field splitting in an approximately octahedral coordination environment.[33]

TABLE II. Seebeck values for the insulating phase of control and irradiated films at 2 MeV in three steps.

Device Resistivity (Ω m)	Substrate	Energy (MeV)	Fluence (ions/cm^2)	S (μV/K)
0.035	SiO_2/Si	Control	0	−236 ± 22
0.034	Al_2O_3 (0001)	Control	0	−9.9 ± 0.2
0.0235	SiO_2/Si	2	5×10^{16}	−51.5 ± 3.2
0.107	Al_2O_3 (0001)	2	5×10^{16}	−27.6 ± 0.9

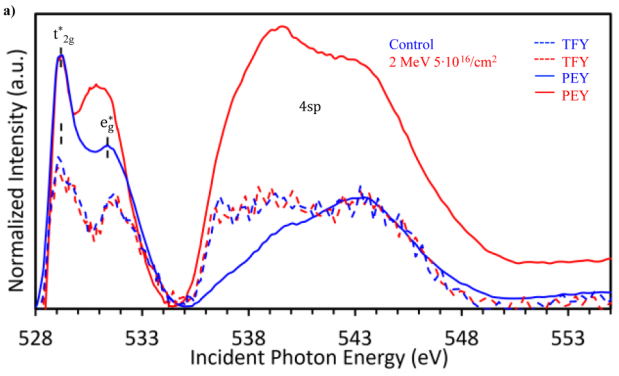

FIG. 5. Oxygen K-edge spectra XANES spectra collected on (a) control (blue) and 2 MeV He irradiated (red) polycrystalline VO_2 on SiO_2/Si. t_{2g} and e_g* features arise from electron transitions, respectively, into lower- and higher energy unoccupied V3d manifolds, while the broad 4sp feature arises from transitions into continuum conduction band states.

We observe larger differences in the PEY spectra, specifically in the intensities of the t_{2g} (π*) and e_g^* (σ*) resonances, which arise from the covalent mixing of empty V 3*d* t_{2g}* and e_g* and filled O 2*p* states. Notably, the broad π* resonance embeds transitions into $d_{||}$ (V $3d_{xy}$) states; the hybridization of these states is strongly modified across the metal–insulator transition of VO_2 because of the Peierls-type dimerization. We further observe that the ratio of t_{2g}^* to e_g^* peak intensities decreases after irradiation, indicating a renormalization of spectral weight from π* to σ* bonds, which is suggesting a decrease in V–O bond covalency and correlated with reduced conductance differential in the MIT (Fig. 5).[34] In the absence of vanadium oxidation state changes, the observed renormalization of spectral weight is consistent with increased electron localization on V-sites due to the local modifications of V/O stoichiometry engendered by the formation of oxygen and vanadium vacancies and subsequent local disorder. Comparison of PEY and TFY data shows considerable surface sensitivity of oxygen stoichiometry variations induced by ion irradiation since the latter spectra show negligible differences.

IV. DISCUSSION

A. Effects of 2 MeV He irradiation on electrical transport

The changes in charge transport behavior in the insulating and metallic phases caused by high energy irradiation can be attributed to either (1) structural changes such as cracks, voids, and the creation of secondary phases or (2) atomic-scale defects induced by the irradiation. The results from both Raman mapping and XRD indicate no significant changes in phase assemblage after high energy irradiation (Fig. S3 in the supplementary material), while TEM images (Fig. S4 in the supplementary material) did not indicate any significant changes in the concentration of microscopic defects (cracks, voids).[12] Thus, we infer that changes in charge transport are primarily attributable to atomic-scale defects, including both point defects and defect clusters.

The trends in the electrical resistivity of the quasi-epitaxial films irradiated with high energy irradiation [Figs. 1(e) and 1(f)] are consistent with the formation of O vacancies.[4] Oxygen vacancies have positive charge, which tends to increase the number of occupied states in the π* and $d_{//}$ bands, causing the Fermi level (E_F) to be shifted toward the conduction band and thereby introducing additional electron carriers.[9] The resulting decrease in the $\rho_{insulating}$ of the quasi-epitaxial film supports this interpretation, as do the Seebeck data showing that transport is dominated by n-type carriers. The MIT in VO_2 is a Peierls–Mott insulator where the transition involves a redistribution of spectral weight driven by strong electronic correlations.[35] While the global MIT and band edges are robust against disorder,[11] defects (such as oxygen vacancies) locally perturb the electronic structure, introducing localized midgap states that influence low-temperature transport.[36,37] Consistent with these results, irradiation in our films does not alter the transition temperature or width. However, the reduced insulating-phase resistivity, increased effective Hall mobility, and enhanced Seebeck coefficient indicate that disorder modifies low-energy electronic states relevant for transport, lowering local activation barriers and improving percolative connectivity between localized conducting regions without affecting the collective Mott–Peierls transition.

TABLE III. Hall measurement values for control and quasi-epitaxial films irradiated at 2 MeV in three steps.

Substrate	Phase (M1 or R)	Fluence (ions/cm^2)	Carrier density (cm^{-3})	Mobility (cm^2/V s)
Al_2O_3 (0001)	M1	0 (control)	2.09×10^{19}	0.1808
Al_2O_3 (0001)	M1	3×10^{16}	2.85×10^{19}	0.347
Al_2O_3 (0001)	R	0 (control)	1.68×10^{23}	0.1926
Al_2O_3 (0001)	R	3×10^{16}	1.47×10^{23}	0.1443

The changes in electrical resistivity can also be explained by the ionization of target atoms (V,O) by the He ions because nearly all the energy from 2 MeV He ions is lost through electronic excitations (99.90%, per SRIM) rather than displacing atoms. This ionization can create oxygen vacancies where defect modified regions led to more connected paths and higher mobilities.

Despite being a complex correlated electron material, Seebeck measurements of the insulating phase are found to be well described by modeling a nondegenerate semiconductor.[20,38] Given the 35% increase in carriers and 93% increase in mobility (Table III) for the insulating phase, it is expected that the Seebeck coefficient (Table II) would decrease instead of tripling in size because, for a nondegenerate semiconductor, a more negative coefficient is characteristic of a Fermi level that is further from the conduction band and consequently has less carriers and a larger resistivity. The increase in the absolute value of the Seebeck coefficient indicates that the Fermi level is moving deeper into the bandgap, which can occur due to the increased localization of carriers because of disorder introduced by irradiation. This localization effect can lead to a situation where despite having more carriers, the effective transport of these carriers is hindered, resulting in a larger Seebeck coefficient. The increase in mobility implies that carriers can move more freely, but the enhanced localization due to disorder may lead to a more pronounced thermoelectric response. Additionally, relaxation times of carriers could also be changing due to disorder. Similar effects were observed in electrical transport and Seebeck data upon low-energy irradiation[12] of quasi-epitaxial films, where the Seebeck coefficient further decreasing was thought to be due to the changing relaxation time of carriers.

Epitaxial strain from thin VO_2/TiO_2 (101) films promotes even carrier redistribution among the $d_{||}$ and π* bands and modifies band curvature, thereby reducing electron effective mass.[39] In a related study, another possible explanation was proposed after alpha particle (He^{2+}) irradiation of VO_2 on Al_2O_3 films at 3 MeV, in which the increase in mobility was attributed to higher electron concentrations spilling electrons into a higher conduction band valley.[40] As a result, these electrons would have higher mobilities due to reduced intervalley scattering or increased damage per ion strike. The decreases in mobility and carrier density in the metallic phase are not as surprising, as carriers are delocalized and the $d_{||}$ and π* bands already overlap, so any changes to the band structure

would see minimal effects. Any added defects or structural changes would mainly introduce scattering in this phase. Thus, upon irradiation of the quasi-epitaxial films, the net result is a more conductive film for the insulating phase.

The electrical resistivity of the polycrystalline films [Figs. 1(a) and 1(b)] varies somewhat after moderate energy irradiation, especially with respect to the increments of irradiation. The resistivity of the insulating phase is minimally affected regardless of the number of irradiation steps—resistivity % change does not scale with dpa. In contrast, we observe a general increase in the electrical resistivity in the metallic phase (up to 217% at the third step), with a single notable exception in two-step irradiation exposure, after which the device behaves closer to the original control measurement (−28%). All three devices measured at this fluence (5×10^{16}), in two steps, responded with a decreased transformation width and a decrease in resistivity for the metallic phase. The sharpened transition and decrease in metallic resistivity both imply that modifications to the electronic states are no longer local and that like the quasi-epitaxial case, there is more connectivity between grains. Irradiation modifies local strain, defect distributions, or domain pinning in a way that promotes more homogeneous and connected metallic domain formation during the transition.[36] The MIT pathway changes and metallic domains nucleate more coherently all while leaving the insulating state and average valence as shown by XANES unchanged.

Analyzing the effects of irradiation performed in three steps, the sharp reduction in the Seebeck coefficient from −236 to −51.5 μV/K (Table II) indicates that exposure to irradiation produced additional carriers and an upward shift of E_F toward the conduction band. A similar reduction in the Seebeck coefficient was observed in W-doped VO_2, with increasing dopant concentration, where doped carriers started to fill the π^* band.[41] Considering that the majority carriers are electrons, this result is consistent with the creation of O vacancies and associated free electrons. While Hall measurements are not available for the polycrystalline films, the relatively unchanged resistivity in the insulating phase, unaltered transformation temperature and width, large reduction in the Seebeck coefficient, and absence of valence changes in XANES indicate a disorder induced localization where long-range connectivity is not improved due to transport being grain boundary

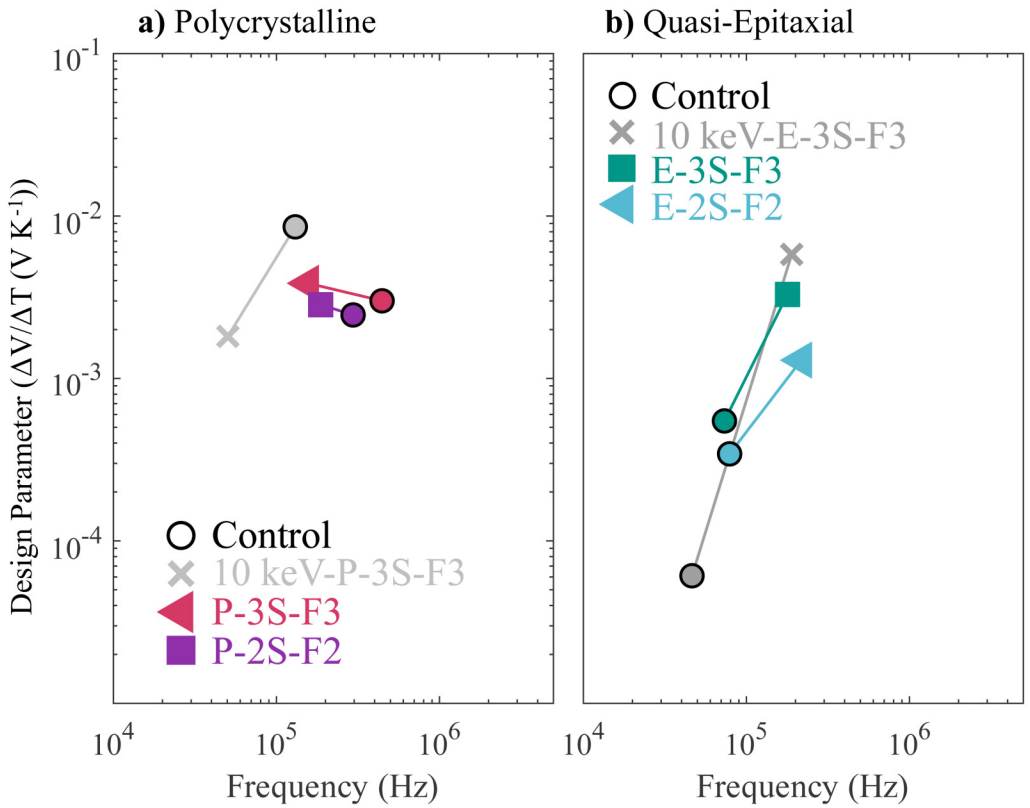

FIG. 6. Performance parameter diagrams, showing the relationship between the design parameter (ΔV/ΔT) for (a) polycrystalline films (P) and (b) quasi-epitaxial (E) control films before irradiation (control) and after low energy (10 keV) and high energy irradiation in three (3 s) and two (2 s) steps. In the legend, the fluence step is specified with F2 for fluence step 2 and F3 for fluence step 3. The nomenclature is discussed in Table I. For comparison, devices are given the lateral device dimensions of L = 40 μm, W = 15 μm, H = 0.1 μm at an ambient temperature of 300 K. Control devices have unfilled markers and are connected via a dotted line to the final irradiation step.

limited.[11,37] The decrease in Seebeck especially indicates that disorder results in a more symmetric electronic transport where high- and low-energy carriers can participate. Irradiation of VO_2 with Ga + ions is consistent with this interpretation where the intrinsic property of resistivity is minimally changed, but local changes are enough to change I–V switching behavior.[36]

As a final observation, we observed that the ρ(T) of the insulating phase is relatively independent of dpa for both types of films [Figs. 1(a) and 1(c)]. Since the film still undergoes a MIT and is not amorphous (confirmed by ρ(T) measurements and structural characterizations), it cannot be attributed to a critical damage point. Thus, it is more likely that the film has reached an equilibrium point between the rate of defects formed and those annihilated by irradiation.

B. Effects of 2 MeV He irradiation on neuronal behavior

The ultimate goal of this research effort is to elucidate the effect that irradiation, and its associated changes in electrical transport properties, has on the performance of oscillators based on VO_2 thin films. To this end, we assessed the comparative effects of both low-energy irradiation (10 keV) from a previous investigation[12] and moderate energy (2 MeV) irradiation on the neuronal behavior of VO_2 devices, as predicted using a physics-based compact model, that translates temperature-dependent electrical and thermal data to simulate neuronal dynamics [Figs. 6(a) and 6(b)].[17] We consider the impact of irradiation on both the operational frequency of a device, assuming a constant device geometry and capacitance, and the performance parameter ΔV/ΔT, which represents the ratio of the voltage amplitude to the magnitude of the temperature pulse associated with a single spike (not to be confused with the Seebeck coefficient). Increasing this parameter corresponds to a greater electrical signal, for a given thermal pulse (quantity of heat dissipation). This model is described in more detail elsewhere.[17]

Overall, irradiation of VO_2 thin films is observed to increase both the operational frequency and ΔV/ΔT for quasi-epitaxial devices [Fig. 6(b)], while having a minimal impact on polycrystalline devices [Fig. 6(a)]. Low energy (10 keV) irradiation results in the greatest changes, especially for the quasi-epitaxial films. In contrast, films irradiated at 2 MeV are clustered together and the frequency of oscillations and ΔV/ΔT parameters do not change as dramatically. To understand the origin of the variation in impact between high and low energy, we further analyzed the differences between low and high energies using SRIM.[15] SRIM can give first-order estimate values on the percent energy loss to ionization and recoils (Fig. S7 in the supplementary material). Ionization (electronic energy) refers to ion energy lost to inelastic collisions between ions and target electrons. Recoil energy (nuclear energy) refers to elastic collisions between target atom nuclei and the incoming ion. Irradiation with 2 MeV He results in the electronic energy dominating with 99.90% of the total energy (1.99 MeV) transferred to electrons and around 1.4 keV transferred to recoils. In contrast, irradiation with 10 keV He results in 7.4 keV (74%) of the total energy transferred to electrons and 2.6 keV (26%) transferred to recoils. Considering the partition of energy, it is not surprising that 10 keV irradiation is more effective in modifying neuronal dynamics as there is a higher recoil energy and higher creation of vacancies by damage. Upon 2 MeV He irradiation, most of the He passes through the film and does not interact significantly with the target VO_2.

V. CONCLUSIONS

This study provides insights into the robustness of VO_2 devices under 2 MeV He irradiation environments and the selectivity of the He irradiation energy to tune the resistivity of the insulating ($\rho_{insulating}$) and metallic ($\rho_{metallic}$) phases without substantially changing the MIT temperature or altering the MIT characteristics. High energy irradiation results in the generation of O vacancies in both types of films, as supported by n-type carriers measured by Seebeck measurements and XANES TFY. In the highly textured films, transport is not strongly limited by grain boundaries, allowing irradiation-induced local reductions in activation barriers to enhance connectivity between pre-existing conducting regions. In contrast, transport in polycrystalline films is dominated by misoriented grain boundaries such that similar local modifications do not translate into improved long-range connectivity. While this is generally true, there are exceptions when considering irradiation history where irradiation in two steps results in a similar response to that of the quasi-epitaxial films.

Physics-based compact models were implemented to simulate electro-thermal oscillations and show that lower energy 10 keV He irradiation tends to be more effective than 2 MeV He irradiation in tuning transport properties for higher oscillation frequencies and signal transmission. At the crux of observed transport trends are differences related to whether incoming kinetic energy of ions is absorbed primarily through ionization (interactions with the target atom's electronic cloud) or recoil processes (displacement of the target atom from its lattice position).[15] Based on these results, low-energy irradiation appears to introduce an additional vector to tune transient oscillation behavior in VO_2 neuromorphic devices.

SUPPLEMENTARY MATERIAL

See the supplementary material for additional information on SEM, AFM, Raman mapping, TEM, XANES, SRIM-based simulations, low-frequency noise measurements, and electrical transport fitting; SEM image of thin film cross section (Fig. S1); AFM of control samples and after the first round of irradiation (Fig. S2); Raman mapping base spectrum and mapping for control and irradiated films (Figs. S3); TEM of control and irradiated samples (Figs. S4); vanadium L-edge XANES of control and irradiated VO_2 on SiO_2/Si samples (Figs. S5); SRIM-based simulations on dpa and resulting He+ concentrations (Fig. S6); SRIM-based simulations for low (10 keV) and high energy (2 MeV) split into recoil and ionization energy (Fig. S7); and low-frequency noise measurements for control and irradiated films (Figs. S8 and Table I).

ACKNOWLEDGMENTS

This work was primarily supported as part of the Center for Reconfigurable Electronic Materials Inspired by Nonlinear

Neuron Dynamics (reMIND), an Energy Frontier Research Center funded by the U.S. Department of Energy, Office of Science, Basic Energy Sciences. VO_2 film growth and characterization were performed at the Texas A&M Engineering Experiment Station under Award No. DE-SC0023353. R.G. acknowledges a graduate fellowship through NSF under Grant No. DGE: 1746932. Film irradiation and device lithography were performed at the Center for Integrated Nanotechnologies, an Office of Science User Facility operated for the U.S. Department of Energy (DOE) Office of Science. Sandia National Laboratories is a multimission laboratory managed and operated by the National Technology & Engineering Solutions of Sandia, LLC, a wholly owned subsidiary of Honeywell International, Inc., for the U.S. DOE's National Nuclear Security Administration under Contract No. DE-NA-0003525. The views expressed in the article do not necessarily represent the views of the U.S. DOE or the U.S. Government.

AUTHOR DECLARATIONS

Conflict of Interest

The authors have no conflicts to disclose.

Author Contributions

Rebeca M. Gurrola: Data curation (equal); Formal analysis (equal); Methodology (equal); Writing – original draft (equal); Writing – review & editing (equal). **Adelaide Bradicich:** Formal analysis (equal); Writing – original draft (supporting); Writing – review & editing (equal). **Fatme Jardali:** Formal analysis (equal); Methodology (lead); Writing – original draft (supporting). **John M. Cain:** Data curation (supporting); Formal analysis (supporting). **Timothy D. Brown:** Data curation (supporting); Formal analysis (supporting). **Jenny L. Chong:** Data curation (supporting); Formal analysis (supporting). **John Ponis:** Data curation (supporting); Formal analysis (supporting). **Sangheon Oh:** Data curation (supporting). **Ryan M. Schoell:** Data curation (supporting). **Digvijay R. Yadav:** Data curation (equal). **Jiaqi Dong:** Data curation (equal). **Christopher M. Smyth:** Data curation (supporting). **Matt Pharr:** Resources (supporting). **Suhas Kumar:** Validation (supporting). **Kelvin Xie:** Resources (supporting). **Sarbajit Banerjee:** Resources (supporting). **Khalid Hattar:** Resources (supporting). **A. Alec Talin:** Resources (supporting); Validation (supporting). **Tzu-Ming Lu:** Formal analysis (supporting); Funding acquisition (supporting); Resources (supporting); Validation (supporting). **Patrick J. Shamberger:** Conceptualization (equal); Formal analysis (equal); Funding acquisition (equal); Resources (equal); Supervision (equal); Validation (equal); Writing – original draft (equal); Writing – review & editing (equal).

DATA AVAILABILITY

The data that support the findings of this study are available from the corresponding author upon request.

REFERENCES

[1]J. L. Andrews, D. A. Santos, M. Meyyappan, R. S. Williams, and S. Banerjee, Trends Chem. **1**, 711 (2019).
[2]T. D. Brown, S. M. Bohaichuk, M. Islam, S. Kumar, E. Pop, and R. S. Williams, Adv. Mater. **35**, 2205451 (2023).
[3]P. Schofield, A. Bradicich, R. M. Gurrola, Y. Zhang, T. D. Brown, M. Pharr, P. J. Shamberger, and S. Banerjee, Adv. Mater. **35**, 2205294 (2023).
[4]C. Chen, Y. Zhao, X. Pan, V. Kuryatkov, A. Bernussi, M. Holtz, and Z. Fan, J. Appl. Phys. **110**, 023707 (2011).
[5]P. Jin, M. Tazawa, K. Yoshimura, K. Igarashi, S. Tanemura, K. Macák, and U. Helmersson, Thin Solid Films **375**, 128 (2000).
[6]P. A. Stolk, H. J. Gossmann, D. J. Eaglesham, D. C. Jacobson, C. S. Rafferty, G. H. Gilmer, M. Jaraíz, J. M. Poate, H. S. Luftman, and T. E. Haynes, J. Appl. Phys. **81**, 6031 (1997).
[7]G. A. Gibson, Adv. Funct. Mater. **28**, 1704175 (2018).
[8]S. Fan, L. Fan, Q. Li, J. Liu, and B. Ye, Appl. Surf. Sci. **321**, 464 (2014).
[9]Z. Zhang, F. Zuo, C. Wan, A. Dutta, J. Kim, J. Rensberg, R. Nawrodt, H. H. Park, T. J. Larrabee, X. Guan, Y. Zhou, S. M. Prokes, C. Ronning, V. M. Shalaev, A. Boltasseva, M. A. Kats, and S. Ramanathan, Phys. Rev. Appl. **7**, 034008 (2017).
[10]D. Lee, B. Chung, Y. Shi, G. Y. Kim, N. Campbell, F. Xue, K. Song, S. Y. Choi, J. P. Podkaminer, T. H. Kim, P. J. Ryan, J. W. Kim, T. R. Paudel, J. H. Kang, J. W. Spinuzzi, D. A. Tenne, E. Y. Tsymbal, M. S. Rzchowski, L. Q. Chen, J. Lee, and C. B. Eom, Science **362**, 1037 (2018).
[11]J. G. Ramirez, T. Saerbeck, S. Wang, J. Trastoy, M. Malnou, J. Lesueur, J.-P. Crocombette, J. E. Villegas, and I. K. Schuller, Phys. Rev. B **91**, 205123 (2015).
[12]R. M. Gurrola, J. M. Cain, S. Oh, T. D. Brown, F. Jardali, R. M. Schoell, D. R. Yadav, J. Dong, C. M. Smyth, M. Pharr, S. Kumar, K. Xie, K. Hattar, A. A. Talin, T.-M. Lu, and P. J. Shamberger, J. Appl. Phys. **135**, 125109 (2024).
[13]E. M. Heckman, L. P. Gonzalez, S. Guha, J. O. Barnes, and A. Carpenter, Thin Solid Films **518**, 265 (2009).
[14]Q. Jia, J. Grenzer, H. He, W. Anwand, Y. Ji, Y. Yuan, K. Huang, T. You, W. Yu, W. Ren, X. Chen, M. Liu, S. Facsko, X. Wang, and X. Ou, Adv. Mater. Interfaces **5**, 1701268 (2018).
[15]J. F. Ziegler, M. D. Ziegler, and J. P. Biersack, Nucl. Instrum. Methods Phys. Res., Sect. B **268**, 1818 (2010).
[16]B. Ravel and M. Newville, J. Synchrotron Radiat. **12**, 537 (2005).
[17]F. Jardali, J. L. Chong, Y. Yu, R. S. Williams, S. Kumar, P. J. Shamberger, and T. D. Brown, Adv. Electron. Mater. **11**, 2400938 (2025).
[18]C. L. Gomez-Heredia, J. A. Ramirez-Rincon, D. Bhardwaj, P. Rajasekar, I. J. Tadeo, J. L. Cervantes-Lopez, J. Ordonez-Miranda, O. Ares, A. M. Umarji, J. Drevillon, K. Joulain, Y. Ezzahri, and J. J. Alvarado-Gil, Sci. Rep. **9**, 14687 (2019).
[19]J. Ordonez-Miranda, Y. Ezzahri, K. Joulain, J. Drevillon, and J. J. Alvarado-Gil, Phys. Rev. B **98**, 075144 (2018).
[20]C. N. Berglund and H. J. Guggenheim, Phys. Rev. **185**, 1022 (1969).
[21]L. Jin, S. E. Zeltmann, H. S. Choe, H. Liu, F. I. Allen, A. M. Minor, and J. Wu, Phys. Rev. B **102**, 041120 (2020).
[22]D. H. Hensler, J. Appl. Phys. **39**, 2354 (1968).
[23]D. Ruzmetov, D. Heiman, B. B. Claflin, V. Narayanamurti, and S. Ramanathan, Phys. Rev. B **79**, 153107 (2009).
[24]C. Wang, H. Zhang, K. Deepak, C. Chen, A. Fouchet, J. Duan, D. Hilliard, U. Kentsch, D. Chen, M. Zeng, X. Gao, Y.-J. Zeng, M. Helm, W. Prellier, and S. Zhou, Phys. Rev. Mater. **3**, 115001 (2019).
[25]A. Herklotz, S. F. Rus, and T. Z. Ward, Nano Lett. **16**, 1782 (2016).
[26]H. Guo, S. Dong, P. D. Rack, J. D. Budai, C. Beekman, Z. Gai, W. Siemons, C. M. Gonzalez, R. Timilsina, A. T. Wong, A. Herklotz, P. C. Snijders, E. Dagotto, and T. Z. Ward, Phys. Rev. Lett. **114**, 256801 (2015).
[27]L. Cao, A. Herklotz, D. Rata, C. Yin, O. Petracic, U. Kentsch, M. Helm, and S. Zhou, Phys. Status Solidi RRL **15**, 2100278 (2021).

[28]A. Moatti, R. Sachan, J. Prater, and J. Narayan, ACS Appl. Mater. Interfaces **9**, 24298 (2017).
[29]L. L. Fan, S. Chen, G. M. Liao, Y. L. Chen, H. Ren, and C. W. Zou, J. Phys.: Condens. Matter **28**, 255002 (2016).
[30]Y. Muraoka, Y. Ueda, and Z. Hiroi, J. Phys. Chem. Solids **63**, 965 (2002).
[31]J. M. Velazquez, C. Jaye, D. A. Fischer, and S. Banerjee, J. Phys. Chem. C **113**, 7639 (2009).
[32]D. Maganas, M. Roemelt, M. Hävecker, A. Trunschke, A. Knop-Gericke, R. Schlögl, and F. Neese, Phys. Chem. Chem. Phys. **15**, 7260 (2013).
[33]P. Schofield, E. J. Braham, B. Zhang, J. L. Andrews, H. K. Drozdick, D. Zhao, W. Zaheer, R. M. Gurrola, K. Xie, P. J. Shamberger, X. Qian, and S. Banerjee, Chem. Commun. **58**, 6586 (2022).
[34]D. Ruzmetov, S. D. Senanayake, V. Narayanamurti, and S. Ramanathan, Phys. Rev. B **77**, 195442 (2008).
[35]T. C. Koethe, Z. Hu, M. W. Haverkort, C. Schüßler-Langeheine, F. Venturini, N. B. Brookes, O. Tjernberg, W. Reichelt, H. H. Hsieh, H. J. Lin, C. T. Chen, and L. H. Tjeng, Phys. Rev. Lett. **97**, 116402 (2006).
[36]N. Ghazikhanian, J. del Valle, P. Salev, R. El Hage, Y. Kalcheim, C. Adda, and I. K. Schuller, Appl. Phys. Lett. **123**, 123505 (2023).
[37]C. Weber, D. D. O'Regan, N. D. M. Hine, M. C. Payne, G. Kotliar, and P. B. Littlewood, Phys. Rev. Lett. **108**, 256402 (2012).
[38]D. Fu, K. Liu, T. Tao, K. Lo, C. Cheng, B. Liu, R. Zhang, H. A. Bechtel, and J. Wu, J. Appl. Phys. **113**, 043707 (2013).
[39]A. D'Elia, V. Polewczyk, A. Y. Petrov, G. Vinai, L. Li, C. W. Zou, S. J. Rezvani, and A. Marcelli, NPG Asia Mater. **16**, 58 (2024).
[40]K. X.-h. Wang, doctoral dissertation thesis (University of California, Berkeley, 2016).
[41]T. Katase, K. Endo, and H. Ohta, Phys. Rev. B **90**, 161105 (2014).